Feature-based Correlation and Topological Similarity for Interbeat Interval Estimation using Ultra-Wideband Radar

Takuya Sakamoto*, *Member, IEEE,* Ryohei Imasaka, Hirofumi Taki, *Member, IEEE,* Toru Sato, *Member, IEEE,*
Mototaka Yoshioka, Kenichi Inoue, Takeshi Fukuda, and Hiroyuki Sakai *Member, IEEE,*

Abstract—The objectives of this paper are to propose a method that can accurately estimate the human heart rate using an ultra-wideband radar system, and to determine the performance of the proposed method through measurements. The proposed method uses the feature points of a radar signal to estimate the heart rate efficiently and accurately. Fourier- and periodicity-based methods are inappropriate for estimation of instantaneous heart rates in real time because heartbeat waveforms are highly variable, even within the beat-to-beat interval. We define six radar waveform features that enable correlation processing to be performed quickly and accurately. In addition, we propose a feature topology signal that is generated from a feature sequence without using amplitude information. This feature topology signal is used to find unreliable feature points, and thus to suppress inaccurate heart rate estimates. Measurements were taken using ultra-wideband radar, while simultaneously performing electro-cardiography measurements in an experiment that was conducted on nine participants. The proposed method achieved an average root-mean-square error in the interbeat interval of 7.17 ms for the nine participants. The results demonstrate the effectiveness and accuracy of the proposed method. The significance of this work for biomedical research is that the proposed method will be useful in the realization of a remote vital signs monitoring system that enables accurate estimation of heart-rate variability, which has been used in various clinical settings for the treatment of conditions such as diabetes and arterial hypertension.

Index Terms—signal processing, heart rate, ultra-wideband radar, signal feature

I. INTRODUCTION

CONTINUOUS and noncontact measurement of human vital signs is an important healthcare technology [1] because such a technology would allow long-term monitoring capabilities to be realized without the attachment of uncomfortable electrodes or sensors to the patient's body. Many studies have been conducted into the development of

*T. Sakamoto is with Graduate School of Engineering, University of Hyogo.
H. Taki is with Graduate School of Biomedical Engineering, Tohoku University.
R. Imasaka and T. Sato are with Graduate School of Informatics, Kyoto University.
M. Yoshioka, K. Inoue, T. Fukuda and H. Sakai are with Advanced Research Division, Panasonic Corporation.

noncontact vital signs monitoring systems using ultrasound [2] and microwaves [2]-[5].

Continuous measurement of respiration is useful in the diagnosis of respiratory disorders such as sleep apnea, and numerous studies have been conducted on this topic [4]-[15]. When compared with respiration, heart rate (HR) measurement requires higher sensitivity to accurately detect target displacement (usually the chest wall movement) that is of sub-millimeter order, whereas the displacement due to respiration is of the order of a few centimeters.

To achieve high sensitivity, continuous wave (CW)-based systems that use motion-modulated phase information are preferable. However, a received CW signal contains not only the signal from the participant, but also stationary clutter, crosstalk from the transmitter, and even signals from other people if there are any in the surrounding area. These effects must be dealt with using direct current (DC) suppression techniques [4], [16], [17] and crosstalk suppression methods with circular polarization [18]. Another approach is the use of an ultra-wideband (UWB) radar system that has high range resolution and thus mitigates the crosstalk and clutter in other range bins. Systems that use impulse radio (IR) have large fractional bandwidths, such as 200% [9], 70% [11] and 60% [12]. These IR systems, however, suffer from relatively low sensitivity to slight motions such as heartbeats.

In this study, we have chosen a radar system that has a relatively narrow fractional bandwidth of 3% (726 MHz 10dB-bandwidth and operating frequency of 26.4 GHz) but is still classified as UWB radar by the US Federal Communications Commission standard because its bandwidth exceeds 500 MHz. This system represents a compromise between CW-based and IR-based systems because it has the high sensitivity of CW-based systems, and the clutter suppression capability of IR-based systems. By finding the correct range bin, this system can obtain clutter-free vital signals without DC component or crosstalk.

The time derivative of the instantaneous HR is called the heart rate variability (HRV). HRV has been proposed as a useful indicator for prevention of sudden cardiac death [19] and diagnosis of stress syndromes [20]. Spectral analysis of the HRV provides two components, the low frequency and high frequency components, which are lower and higher than 0.15 Hz, respectively. The ratio of these components provides

crucial information for sympatho-vagal balance evaluation [2], [21]. For this purpose, it is essential to estimate the instantaneous HR or its inverse number, the inter-beat interval (IBI), in real time.

There are four distinct approaches for HR estimation: the periodicity-based approach, the Fourier-based approach, the template-waveform-based approach and the feature-based approach. The first approach assumes the periodicity of the vital signs. Conte et al. [22] proposed a maximum likelihood period estimator that can accurately estimate the periodicity of an arbitrary periodic signal. However, the problem with this method is that real vital signals are not always periodic. The second approach is based on Fourier analysis, wherein a signal is modeled as a summation of sinusoidal waves. Fourier-based methods include the use of well-known periodograms [5], [8], [12], [17], spectrograms [23], and parametric methods such as the maximum entropy method (MEM) [20] and the RELAX algorithm [24]. The third approach requires a reference signal that provides a template waveform. A received signal is then modeled as a summation of these template waveforms with various coefficients and delays [20], [21]. The challenge in using this type of approach is that it is not always easy to compose an ideal template waveform from real measurement data.

The fourth approach uses feature points of the signals, and this paper is categorized in that group. Several studies have used this approach implicitly. The most common way to analyze the correlation between electrocardiogram (ECG) data and microwave data is via a comparison of the waveform peaks [17], [25], [26], which are among the main signal features. Hu et al.[16] estimated the HR using the zero-crossings of a radar signal after application of various signal processing techniques. In this case, zero-crossings were chosen as a feature for IBI estimation.

This paper extends the fourth approach, and uses the feature points of radar signals to estimate IBIs accurately. First, we define six types of feature points from a radar signal. Second, we propose an efficient IBI estimation method that only calculates a correlation for a small number of time lags that corresponds to matched feature points. Third, we use the topological information from the signal features to reject any unreliable features. Finally, the proposed methods are applied to measurement data taken from nine test participants to demonstrate the effectiveness of the proposed method. For this purpose, we performed simultaneous measurements using ultra-wideband radar and an ECG device.

II. MEASUREMENT SETUP AND PREPROCESSING

The radar equipment used in this study generates signals with a center frequency of 26.4 GHz and an occupied bandwidth (99%) of 780 MHz. The transmitted signal is modulated by a pseudo-noise (PN) sequence, composed of an m-sequence of 500 chip/s. The receiver uses the same PN sequence to demodulate the received signal; this process is also called pulse compression. The pulse-compressed signal is then down-converted and sampled to obtain in-phase (I) and quadrature (Q) signals with a fast-time sampling interval $\Delta t_{\rm f}$ of 2 ns,
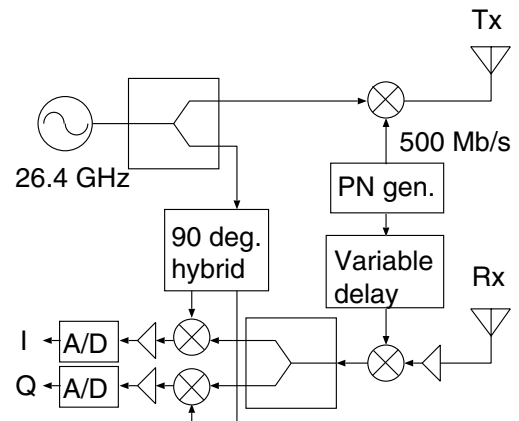

Fig. 1. Block diagram of the measurement system.

TABLE I
BIOMETRIC DATA OF THE TEST PARTICIPANTS.

Metrics	Mean $\pm$ STD
Age	23.3 ± 1.6 years
Weight	61.4 ± 8.9 kg
Height	173.4 ± 6.1 cm
BMI	20.4 ± 2.0 kg/m^2

which corresponds to a range bin size of 30 cm. The range measurement interval Δt is 1.285 ms, which corresponds to the time resolution of a slow time. Hereafter Δt denotes as the sampling interval. A block diagram of the radar system is shown in Fig. 1. We used two horn antennas that have 3-dB beam-widths of $\pm 11°$ in both the E- and H-planes.

It should be noted here that the frequency band (26 GHz) used in this study has been adopted for automotive short range radar (SRR) sensors in both Europe and the USA. We originally developed a 26 GHz radar system [27] for use in automotive SRR system applications. In this paper, however, we use the same radar system for a different purpose: vital signs monitoring.

We took data from nine healthy test participants using a protocol that is approved by the Kyoto University Graduate School and the Faculty of Medicine's Ethics Committee. The participants were all male with ages ranging between 21 and 27; this is largely because the participants were selected from students of the Engineering department, where most of

TABLE II
MEASURED AND ESTIMATED HEARTBEAT INTERVAL RESULTS FOR TEST PARTICIPANTS.

Participant	$T_{\rm obs}$ [s]	IBI$_{\rm min/max}$ [s]	HR$_{\rm ave}$ [bpm]
1	20	0.68/0.80	79.0
2	50	0.50/0.86	77.0
3	55	0.95/1.22	52.7
4	55	0.57/0.71	91.2
5	55	0.68/1.01	62.8
6	55	0.83/0.95	65.9
7	52	0.67/1.08	59.8
8	40	0.91/1.06	59.8
9	30	0.58/0.83	79.0

Fig. 2.   Measurement setup with test participant sitting in a chair with a backrest.

Fig. 3.   Raw data of ECG voltage (black) and radar phase signal (red).

the students are young males. The biometric statistical data from these participants are shown in Table I. The highest and lowest body mass indexes (BMIs) were 22.9 and 17.6, respectively; these values are lower than the average BMI because all participants are of East Asian origin and are thus likely to have a relatively low BMI, especially if they are young and male. The participants were clothed normally during the measurements. We asked the participants to take off any jackets, but did not impose any restrictions on the type of clothing worn.

The test participants remained seated in a chair with their back in contact with the backrest (see Fig. 2), facing the radar antennas. The participants were instructed to hold their breath and remain still during each measurement. Both antennas were directed towards each participant's chest, such that the main lobe of the beam pattern was directed at the pit of the subject's stomach. The duration of each measurement varied from 20 to 55 s, depending on the length of time that each participant could hold their breath. Table II shows the measurement duration T_{obs}, the minimum and maximum IBIs $\mathrm{IBI}_{\mathrm{min/max}}$, and the average HR of each participant $\mathrm{HR}_{\mathrm{ave}}$.

A complex radar signal is denoted by $s_0(t,r)$, where the real and imaginary parts are the I and Q channel outputs, t is a slow time, and r is the range $r = ct_{\mathrm{f}}/2$ corresponding to a fast time t_{f}, where c is the speed of a radiowave. We detect the range r_0 by finding the maximum signal intensity $r_0 = \arg\max_r \int |s_0(t,r)|^2 \mathrm{d}t$ to locate the target range. Then, we apply an arctangent demodulation [3], [10], [23], [24] to obtain the phase of the signal $s_{\mathrm{p}}(t) = \angle s_0(t, r_0)$. The phase is defined here such that a larger phase value corresponds to a longer distance between the antenna and the target.

For comparison, we also measured the ECG using a wireless ECG device (RF-ECG EK, Micro Medical Device, Inc., Tokyo, Japan). The device samples the voltage between a pair of electrodes attached to the chest of the test participant with a sampling frequency of 204 Hz. The ECG data measured using this device are used for reference to evaluate the accuracy of the radar measurements. We detect the time intervals between adjacent R-waves for comparison with the IBI estimates using radar signals.
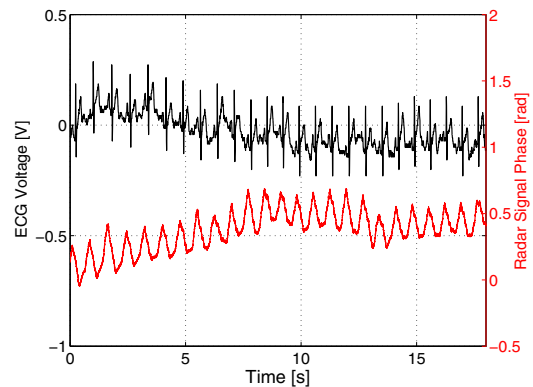
Figure 3 shows an example of an ECG signal and a radar signal phase $s_{\mathrm{p}}(t)$ that were measured simultaneously. Their peaks seem to be synchronized, and this will be quantitatively analyzed later. The peak-to-peak amplitude of the radar signal phase is approximately 0.35 rad, which corresponds to a target displacement of 0.63 mm when considering the center wavelength of 11.4 mm.

The phase signal $s_{\mathrm{p}}(t)$ contains a trend component that is caused by unintentional body movement. We estimate this trend $s_1(t)$ by smoothing $s_{\mathrm{p}}(t)$ using a Gaussian function that is denoted by

$$g_\sigma(t) = \frac{1}{\sqrt{2\pi\sigma^2}} \exp\left(\frac{-t^2}{2\sigma^2}\right), \qquad (1)$$

where σ is a scaling parameter. The smoothing can then be written as

$$s_\sigma(t) = g_\sigma(t) * s_{\mathrm{p}}(t), \qquad (2)$$

where the symbol $*$ is a convolution operator. To estimate the signal trend, $\sigma = \sigma_0$ must be larger than a typical heartbeat interval. In this study, we chose $\sigma_0 = 1.285$ s which corresponds to a HR of 47 bpm; this value lower than a typical HR. This trend, $s_{\sigma 0}(t)$, is subtracted from $s_{\mathrm{p}}(t)$, and a smoothing technique is then applied to obtain $s(t) = (s_{\mathrm{p}}(t) - s_{\sigma 0}(t)) * g_{\sigma 1}(t)$. We chose a smoothing length of $\sigma_1 = 6.4$ ms in this study. Hereafter the signal $s(t)$ denotes the radar signal.

III. Signal Features and Estimating Heart Rate

Wang et al. [28] discussed some feature points of the radar signal, but these feature points were not used quantitatively in their analysis. Hu et al. [16] used the zero-crossings of a processed radar signal to estimate HRs. Mikhelson et al. [17] indicated that the peaks of a radar signal are synchronized with the corresponding ECG signal. In this way, certain feature points have attracted attention in some studies. However, these have not been used systematically for HR estimation.

First, let us define the feature points that are used in later sections for IBI estimation. The features used in this study are

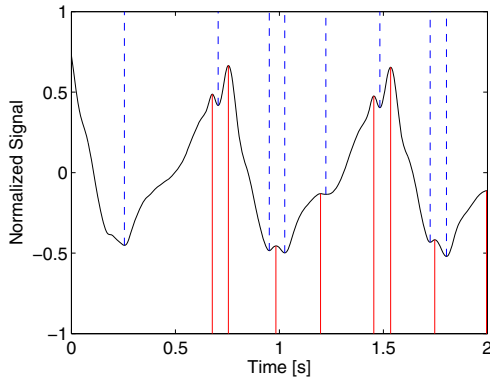- PK: peaks satisfying $\mathrm{d}s(t)/\mathrm{d}t = 0$ and $\mathrm{d}^2 s(t)/\mathrm{d}t^2 < 0$,
- VL: valleys satisfying $\mathrm{d}s(t)/\mathrm{d}t = 0$ and $\mathrm{d}^2 s(t)/\mathrm{d}t^2 > 0$,

Fig. 4. Radar signal $s(t)$ with feature points of PKs (solid red lines) and VLs (dashed blue lines).

Fig. 5. Differentiated radar signal $\mathrm{d}s(t)/\mathrm{d}t$ and feature points, including RDPs and FDPs (solid red lines) and RDVs and FDVs (dashed blue lines).

- RDP: rising derivative peak $\mathrm{d}s(t)/\mathrm{d}t > 0$, $\mathrm{d}^2 s(t)/\mathrm{d}t^2 = 0$ and $\mathrm{d}^3 s(t)/\mathrm{d}t^3 < 0$,
- RDV: rising derivative valley $\mathrm{d}s(t)/\mathrm{d}t > 0$, $\mathrm{d}^2 s(t)/\mathrm{d}t^2 = 0$ and $\mathrm{d}^3 s(t)/\mathrm{d}t^3 > 0$,
- FDP: falling derivative peak $\mathrm{d}s(t)/\mathrm{d}t < 0$, $\mathrm{d}^2 s(t)/\mathrm{d}t^2 = 0$ and $\mathrm{d}^3 s(t)/\mathrm{d}t^3 < 0$, and
- FDV: falling derivative valley $\mathrm{d}s(t)/\mathrm{d}t < 0$, $\mathrm{d}^2 s(t)/\mathrm{d}t^2 = 0$ and $\mathrm{d}^3 s(t)/\mathrm{d}t^3 > 0$.

Figure 4 shows an example of a radar signal $s(t)$ and the detected peaks (PK) and valleys (VL) are displayed in red and blue, respectively. In this figure, we can see that there are two peaks that are located close to each other (a pair at around $t = 0.7$ s and $t = 1.5$ s) in each cycle. These double peaks are occasionally found in radar signals, and have also been observed by other researchers in the literature; for example, see Fig. 6 of [20] and Fig. 11 (c) of [17]. The existence of these double peaks indicates that simple peak detection is insufficient for accurate HR estimation, because such a method might detect the wrong one of the two peaks.

Figure 5 shows the time-derivative $\mathrm{d}s(t)/\mathrm{d}t$ of the signal in Fig. 4. Four feature points RDP, RDV, FDP and FDV are also displayed using solid red lines (RDP and FDP) and dashed blue lines (RDV and FDV). In this way, we can obtain limitless numbers of feature points by differentiating the original signal with respect to time multiple times. However, a higher-order derivative emphasizes the higher frequency components, and this makes the use of this derivative impractical for actual noisy signals. Therefore, we detect and use these six features in this paper.

IV. FEATURE-BASED CORRELATION FUNCTION

We detect the feature points PK, VL, RDP, RDV, FDP, and FDV sequentially, and then store them in a sequence f_n $(n = 1, \cdots, N)$. The time and type of a feature point f_n are denoted by τ_n and g_n, respectively, where $g_n \in \{\mathrm{PK, VL, RDP, RDV, FDP, FDV}\}$. The feature points are arranged in ascending order as $\tau_1 < \tau_2 < \cdots < \tau_N$.

For each feature point, the first task is to find the next feature point that has the highest correlation. The feature point must also have the same feature type g_n. We call this feature point
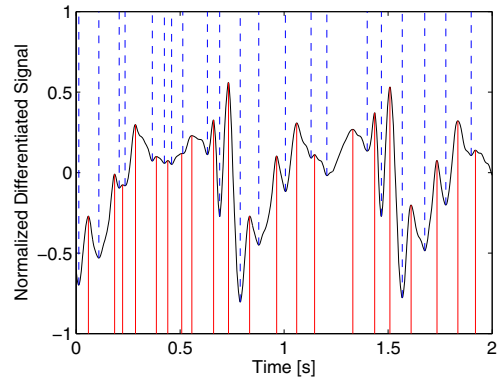
an associated feature point, with an index that is denoted by $\hat{m}_n$. We perform this process by calculating the local cross-correlation function. First, we define a $(2K + 1) \times 1$ vector composed of the signal samples around the n-th feature point as

$$\overline{\boldsymbol{v}}_n = [s(\tau_n - K\Delta t), s(\tau_n - (K-1)\Delta t), \cdots, s(\tau_n + K\Delta t)]^{\mathrm{T}}, \quad (3)$$

where Δt is the sampling interval. We determine K using $K\Delta t = T_{\mathrm{c}}/2$ where T_{c} is the time span to calculate a correlation. The DC component is subtracted as

$$\boldsymbol{v}_n = \overline{\boldsymbol{v}}_n - \frac{1}{2K+1} U\overline{\boldsymbol{v}}_n, \quad (4)$$

where U is a $(2K + 1) \times (2K + 1)$ matrix that contains 1s in all its elements. The correlation $c_{m,n}$ between the m-th and n-th feature points is defined as

$$c_{m,n} = \frac{\boldsymbol{v}_n^{\mathrm{T}} \boldsymbol{v}_m}{|\boldsymbol{v}_n|\,|\boldsymbol{v}_m|}, \quad (5)$$

if the feature points are of the same kind, where $g_n = g_m$. The correlation $c_{m,n}$ is defined to be zero when $g_n \neq g_m$.

For each feature point n, its associated feature point $\hat{m}_n$ is defined as

$$\hat{m}_n = \max_{m > n} c_{m,n}. \quad (6)$$

We can then estimate the IBI, or the instantaneous HR, as

$$h\left((\tau_{\hat{m}_n} + \tau_n)/2\right) = \tau_{\hat{m}_n} - \tau_n, \quad (7)$$

where $h(t)$ is the IBI at time t, and the time is defined as the midpoint between two corresponding feature points in this paper. Unlike conventional correlation functions, this method only calculates the correlation values for a few possible combinations of feature points. For example, a typical heartbeat signal $s(t)$ has only a few peak points every second. Assuming that the test participant has a normal heart rate, the correlation integral only needs to be performed a few times for each feature point, and this is even faster than using a fast Fourier transform-based auto-correlation function. This means that the proposed method is much faster than conventional methods.

The black curve at the bottom of Fig. 6 is an example of the radar signal $s(t)$, and its local correlation function for
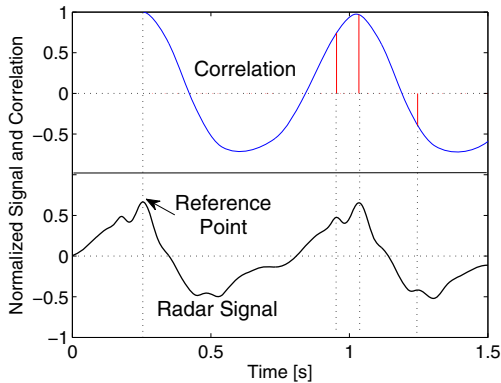
Fig. 6. A radar signal (lower black curve), its local auto-correlation function (upper blue curve) and correlation coefficients evaluated using the proposed method (red lines).
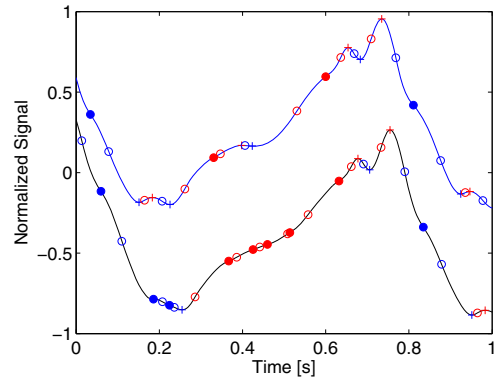

Fig. 7. Radar signal and feature points. PK, VL, RDP, RDV, FDP, and FDV are marked with a red cross, a blue cross, a red circle, a red-filled circle, a blue-filled circle, and a blue circle, respectively.

the reference feature point (PK) at $t = 0.25$ s is shown as the blue curve at the top. Here, we set the window width for the correlation process to be $T_c = 1.8$ s, which covers an entire cycle of a normal heartbeat waveform. The three red lines indicate the correlation values that were calculated using our proposed method. There are only three matched feature points (PKs) with time lags in the range between 0.5 and 1.3 s that correspond to HRs of between 45 and 120 bpm, respectively. In this way, the proposed method limits the number of correlation values that have to be evaluated, which enables the fast computation required in realtime applications.

V. FEATURE TOPOLOGY SIMILARITY FOR SELECTING FEATURE POINTS

In the previous section, we proposed an efficient IBI estimation method using the feature points found in a waveform. However, not all detected features can be used for IBI estimation because the waveform can even change within the duration of a pulse-to-pulse interval. Figure 7 shows an example of a signal with two cycles. The second cycle is shifted to be above the first and is then superposed for ease of comparison. The first and second cycles are represented by the black and blue lines, respectively. In the figure, along with the signal waveforms, the detected feature points are also shown: the PK, VL, RDP, RDV, FDP, and FDV are marked with a red cross, a blue cross, a red circle, a red-filled circle, a blue-filled circle, and a blue circle, respectively.

It is observed that the feature points located around the peaks show higher reproducibility than the points located around the valleys. The feature point sequence around the peaks is RDP-RDV-RDP-PK-FDV-VL-RDP-PK-FDV-FDP-FDV for both cycles. In contrast, the feature point sequences around the valleys are not consistent, with FDP-FDV-FDP-FDV-FDP-FDV-VL-RDP-RDV for the first cycle, and FDP-FDV-VL-RDP-PK-FDV-VL-RDP-RDV for the second cycle. From this observation, we conclude that we need to find reliable feature points that are consistent over at least a few cycles. To perform pattern matching of these sequences, the
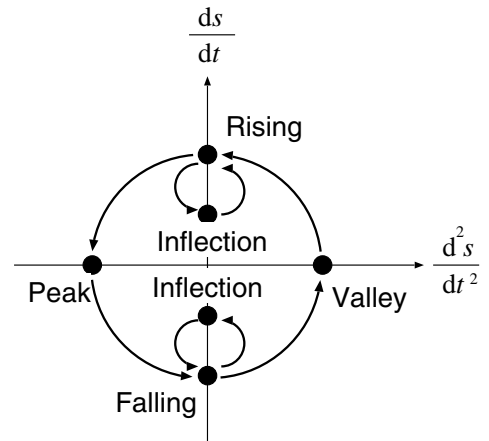

Fig. 8. Schematic of state space representation of a radar signal measuring heartbeats.

similarity of the sequences must be evaluated using topological information rather than their waveform correlations.

We introduce a new approach to evaluate the topological similarities of sequences. The six feature points (PK, VL, RDP, RDV, FDP, and FDV) can be displayed schematically on a state space with axes of d^2s/dt^2 and ds/dt (see Fig. 8). If a signal is sinusoidal, then the state vector moves along the outer circle in the figure, because for a signal $s(t) = \cos(\omega t + \theta)$,

$$\left[\begin{array}{c} d^2s/dt^2 \\ ds/dt \end{array} \right] = -\omega \left[\begin{array}{c} \omega \cos(\omega t + \theta) \\ \sin(\omega t + \theta) \end{array} \right]. \qquad (8)$$

The actual radar signal, however, has some inflection points that correspond to the two additional states shown inside the circle in Fig. 8.

Inspired by this, we generate a feature topology signal $s_t(t)$, which has a complex value, from the original signal $s(t)$. $s_t(t)$ does not contain signal intensity information, because that information is already used in the feature-based correlation method that was introduced in the previous section. For the n-th feature point f_n, $s_t(\tau_n)$ can take a complex number form, depending on the type of feature g_n. In this case, $s_t(\tau_n)$ is set to be 1, j, $-j/2$, -1, $-j$, and j/2 for VL, RDP, RDV, PK, FDV,

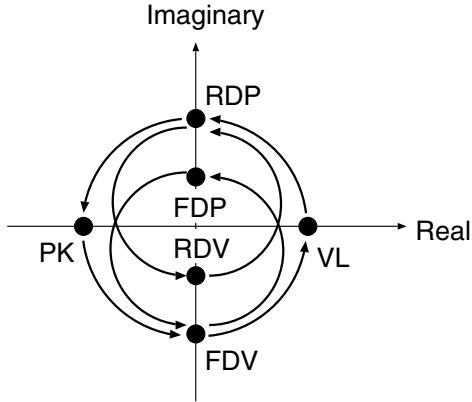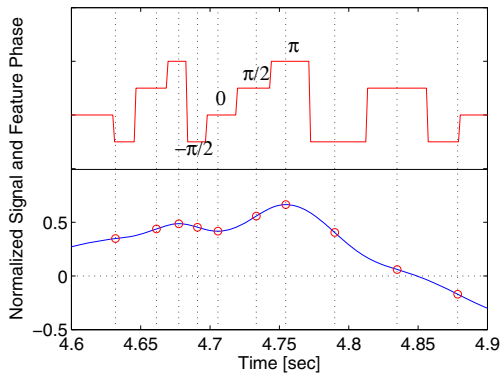Fig. 9. Complex value assigned to each feature point.
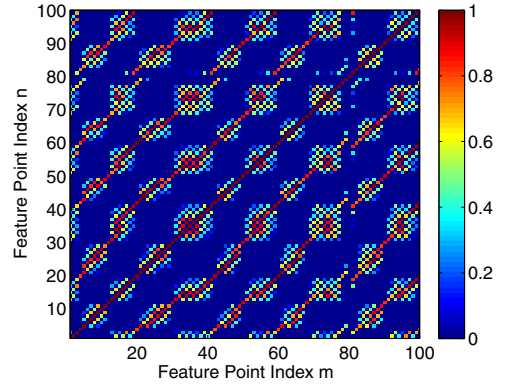

Fig. 11. Self-similarity matrix of feature topology signal using the phase assignment, as shown in Fig. 8.

Fig. 10. Example of feature phase signal.
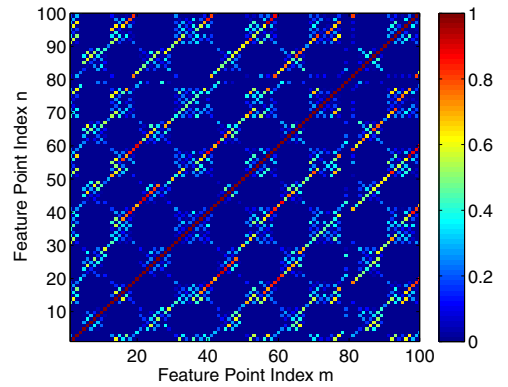

Fig. 12. Self-similarity matrix of feature topology signal using the proposed phase assignment, as shown in Fig. 9.

and FDP, respectively. The proposed assignment of complex values is illustrated in Fig. 9. For $t \neq \tau_n$, $s_t(t)$ takes the value of the closest feature point, which means that $s_t(t) = s_t(\tau_L)$, where L is found from $L = \arg\min_l |\tau_l - t|$. Note that the complex values for both RDV and FDP have opposite signs to the corresponding points shown in Fig. 8. This is because the proposed assignment has higher sensitivity when calculating the cross-correlation. This can be understood by recalling that in Fig. 7, the feature point pairs RDP-RDV and FDV-FDP were often observed alternately. We use this characteristic to improve the matching accuracy of our algorithm.

We show an example of the angle of a feature topology signal, $\angle s_t(t)$ in Fig. 10. In the lower part of the figure, the original signal $s(t)$ and its feature points f_n $(n = 1, \cdots, N)$ are shown as a blue line and red circles, respectively. The red line in the upper part of the figure displays the phase of the feature topology signal. We see that the phase remains constant around each feature point.

Let us define the self-similarity matrix (SSM) M of the topology signal $s_t(t)$. The (m, n)-th element of M is defined to be the local correlation between two feature points, f_m and f_n as

$$M_{m,n} = \frac{\left| \boldsymbol{u}_m^{\mathrm{H}} \boldsymbol{u}_n \right|^2}{\left| \boldsymbol{u}_m \right|^2 \left| \boldsymbol{u}_n \right|^2}, \tag{9}$$

where $\cdot^{\mathrm{H}}$ denotes the Hermitian transpose operator, and the complex vector $\boldsymbol{u}_n$ is a vector for the n-th feature point and is defined as

$$\boldsymbol{u}_n = [s_t(\tau_n - K_t\Delta t), s_t(\tau_n - (K_t - 1)\Delta t), \cdots, s_t(\tau_n + K_t\Delta t)]^{\mathrm{T}}, \tag{10}$$

where $K_t\Delta t = T_t/2$.

Figures 11 and 12 show examples of SSMs M using a measured signal from a participant. The former and latter were generated using two different phase assignments: a simple assignment of 1, j, j/2, −1, −j, −j/2 for VL, RDP, RDV, PK, FDV, and FDP, and the proposed assignment as shown in Fig. 9. We see only blurred blobs in Fig. 11, whereas Fig. 12 shows clearer lines, which means that the proposed phase assignment provides better resolution of the topological similarity. Note that we only calculated the SSMs above for comparative display. The actual proposed method calculates the topological similarities for the associated feature indices n and $\hat{m}_n$. Therefore, the SSM does not need to be calculated during the actual processing, which means that the topological similarities can be calculated quickly.

Figure 13 compares the feature topological similarity with the waveform correlation that has already been shown in Fig. 6. The feature topological similarity is shown in black in the upper part of the figure. The topological similarity
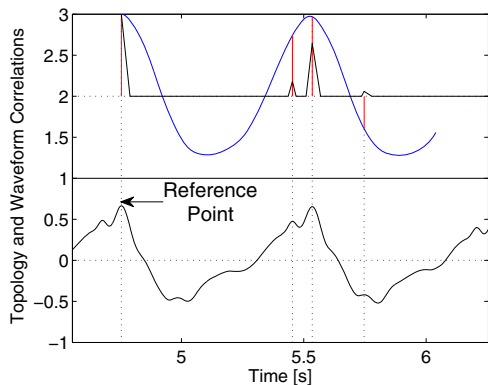
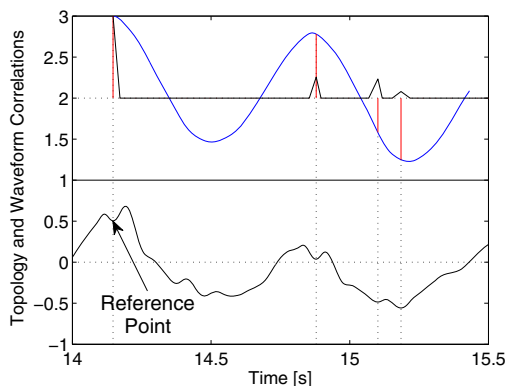Fig. 13. Case when correlation and topological similarity are consistent.

Fig. 14. Case with high correlation and low topological similarity. The topological similarity detected the deformation of the waveforms.

has its largest value when the correlation value is also large. We show another example in Fig. 14, in which waveform deformation is observed; the second waveform is distorted when compared with the first. While the correlation value is relatively high, the feature topology similarity gives a lower value, and thus successfully detects the deformation of the waveform. Therefore, by using the feature topology similarity and a suitable threshold, we can eliminate the unreliable feature point pairs.

VI. PROCEDURE OF THE PROPOSED METHOD

The proposed method is performed using the following procedure.

1) Obtain the phase signal $s_{\mathrm{p}}(t) = \angle s_0(t, r_0)$, where $r_0 = \arg\max_r \int |s_0(t, r)|^2 \mathrm{d}t$.
2) Estimate a trend $s_1(t) = g_{\sigma 0}(t) * s_{\mathrm{p}}(t)$ by smoothing.
3) Subtract the trend from the phase signal and apply smoothing as $s(t) = (s_{\mathrm{p}}(t) - s_1(t)) * g_{\sigma 1}(t)$.
4) Extract the feature points from $s(t)$, $\mathrm{d}s(t)/\mathrm{d}t$, and $\mathrm{d}^2 s(t)/\mathrm{d}t^2$.
5) For each feature point n, calculate the correlation value $c_{m,n}$ using Eqs. (3)-(5).
6) Find the associated feature point $\hat{m}_n$ using Eq. (6) if $\max_m c_{m,n} > \theta_{\mathrm{c}}$.

7) For each pair of associated feature points n and $m = \hat{m}_n$, check their feature topology similarity $M_{m,n}$ using Eqs. (9) and (10).
8) If $M_{m,n} > \theta_{\mathrm{t}}$, calculate the IBI using Eq. (7).
9) Apply a median filter of length N_{m} to the IBI sequence, followed by smoothing with correlation length σ_2 to obtain the final IBIs.

We set $\sigma_0 = 1.285$ s, $\sigma_1 = 6.4$ ms, $\sigma_2 = 0.2$ s, $T_{\mathrm{c}} = 1.8$ s, $T_{\mathrm{t}} = 0.3$ s, $\theta_{\mathrm{c}} = 0.1$ and $\theta_{\mathrm{t}} = 0.7$ and $N_{\mathrm{m}} = 11$. When searching for the maximum $c_{m,n}$, we assume that the IBI should be between 0.5 and 1.3 s, which corresponds to an HR of between 120 and 45 bpm.

Although we have proposed a method with $\theta_{\mathrm{c}} = 0.1$ and $\theta_{\mathrm{t}} = 0.7$, we must also vary these values to clarify the effectiveness of the combined use of the correlation $c_{m,n}$ and the feature topology similarity $M_{m,n}$. In the next section, we compare the performance of the proposed method with two other simplified methods: in the first, $\theta_{\mathrm{c}} = 0.1$ and $\theta_{\mathrm{t}} = 0.0$ and in the second, $\theta_{\mathrm{c}} = 0.7$ and $\theta_{\mathrm{t}} = 0.0$. These simplified methods in practice do not use the feature topology when we set $\theta_{\mathrm{t}} = 0.0$. The first method with $\theta_{\mathrm{c}} = 0.1$ maintains a low threshold that leads to a low rejection ratio, which means that even if the waveform correlation is as low as 0.1, we trust the associated feature point. In contrast, the second method rejects any correlation values lower than $\theta_{\mathrm{c}} = 0.7$, which leads to stricter feature point selection.

VII. ACCURACY EVALUATION OF THE PROPOSED METHOD

In this section, we apply the proposed method to actual radar data that were measured simultaneously with the ECG measurements for the nine participants. Figures 15 and 16 show the IBIs that were estimated using the proposed method and the ECG data for participants 2 and 4, respectively. These results illustrate the remarkable performance of the proposed method. The estimate shown in Fig. 15 does not follow the IBI of the ECG accurately when the HR changes abruptly in the period from 25 to 30 s, which results in a relatively large error. The estimate shown in Fig. 16 is good, apart from the errors observed at $t = 30$ s. Figure 17 shows the radar signal $s(t)$ for participant 4, in which we see a sudden jolt at around $t = 30$ s. This is the reason why the estimated IBI is inaccurate in Fig. 16 during the same time period. Apart from these irregular sections, the proposed method is able to estimate the IBI accurately overall.

Because one of the purposes of this study is the development of a method to monitor HRV, we now give an example involving the participant with the largest heart rate variability. Fig. 18 shows the IBIs that were estimated using both the proposed method and the ECG data for participant 7, who had the longest and shortest IBIs 0.67 s and 1.08 s, respectively. As shown in this figure, the proposed method can accurately estimate even dynamically changing IBIs. The RMS error in IBI estimation for this participant is 7.9 ms.

In the proposed method, we use six types of waveform features, while many existing technologies [17], [25], [26] only use the waveform peaks to estimate the IBIs. For comparison,
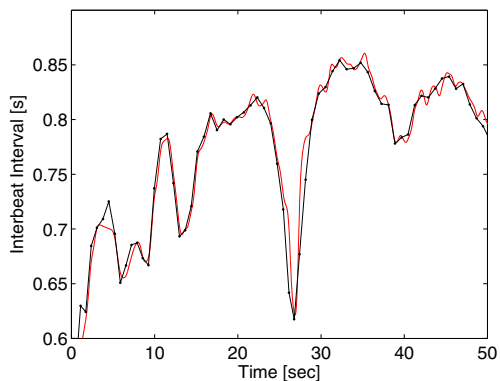
Fig. 15. IBIs estimated from the ECG (black) and the radar signal (red) using the proposed method for participant 2.
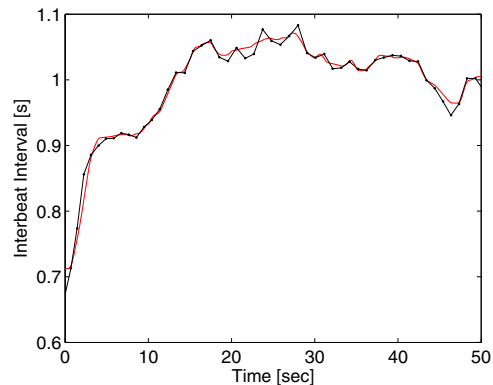

Fig. 18. IBIs estimated from the ECG (black) and radar (red) signal using the proposed method for participant 7.
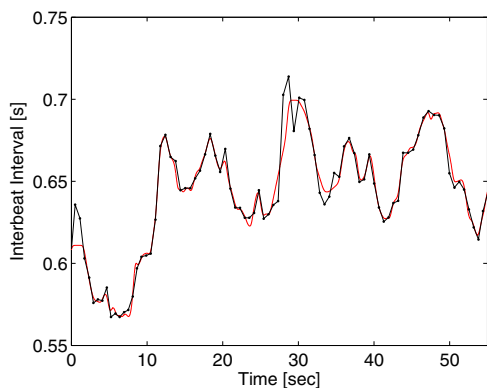

Fig. 16. IBIs estimated from the ECG (black) and the radar signal (red) using the proposed method for participant 4.
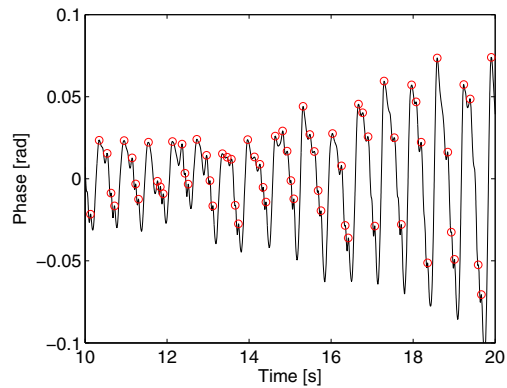

Fig. 19. Zoomed section of radar signal $s(t)$ for participant 4, showing the signal peaks.

let us show part of the radar signal $s(t)$ for participant 4 and its peaks in Fig. 19, where the signal is the same as that shown in Fig. 17. The waveforms are shown to be so complicated that IBI estimation from the peaks is a difficult task. To avoid this problem, we apply a smoothing technique (Eq. (2)) with $\sigma = 65.0$ms to the raw radar signal and then calculate the peaks (see Fig. 20). In this case, each cycle

Fig. 17. Radar signal $s(t)$ for participant 4.

appears to have only a single peak, which makes the IBI estimation process easier. The IBIs that were estimated using the ECG, the proposed method, and the peaks in Fig. 20 are shown as black circles, red lines, and blue dashed lines in Fig. 21, respectively. The accuracy of the IBIs that were estimated using the peaks is lower than that of the IBIs that were estimated using the proposed method. This is because the multiple small peaks shown in Fig. 19 are averaged by the smoothing technique, and the detailed information contained in the waveform was spoiled. In this way, the use of multiple feature points is shown to be useful for accurate IBI estimation.
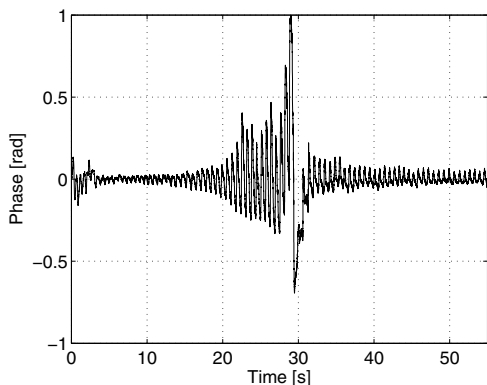
Figure 22 shows the RMS error of the estimated IBIs, where the error is defined as the difference between the IBIs estimated from the radar signal and those estimated from the ECG data. In this figure, we also applied the two simplified methods with different parameters. The thresholds are set to be $(\theta_c, \theta_t) = (0.1, 0.0)$, $(\theta_c, \theta_t) = (0.7, 0.0)$, and $(\theta_c, \theta_t) = (0.1, 0.7)$, where the last is for the proposed method. In this figure, we see that the proposed method (in red) gives the smallest error of 7.17 ms on average over the nine participants, while the other two methods (shown in blue and green) give errors of 13.6 and 12.6 ms; this means that the proposed method can estimate IBIs more accurately than the two methods that do not use the feature topology by 90.1
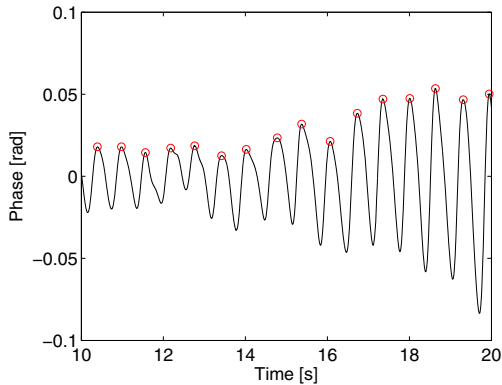
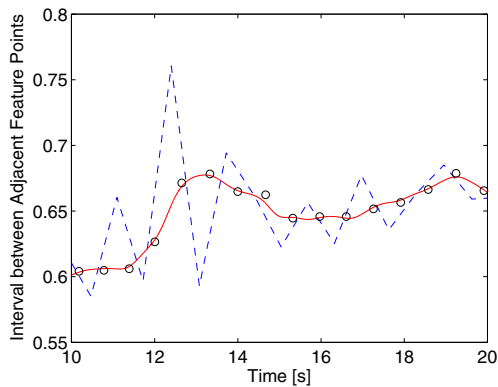Fig. 20. Smoothed radar signal with $\sigma = 65.0$ms for participant 4 showing the signal peaks.

Fig. 22. RMS error of IBIs estimated using the proposed method (in red) with $(\theta_c, \theta_t) = (0.1, 0.7)$, compared with the errors of correlation-based methods with $(\theta_c, \theta_t) = (0.1, 0.0)$ (in blue) and $(\theta_c, \theta_t) = (0.7, 0.0)$ (in green).

Fig. 21. IBIs estimated using the ECG data (black circles), the proposed method (red), and the conventional peak-based method (blue).

Fig. 23. Scattering diagram of IBIs derived from ECG and radar data using the proposed method (black) and the simplified method without use of topology information (red) for participant 6.

and 76.4 %, respectively.

Figure 23 shows the scattering diagram of the IBIs that were estimated from the ECG data and the radar signal for participant 6. The black and red plots indicate the results for the proposed method with $(\theta_c, \theta_t) = (0.1, 0.7)$ and for a method without use of topology information with $(\theta_c, \theta_t) = (0.1, 0.0)$, respectively. It is observed that the proposed method provides a higher correlation between the two data sets. This comparison can be evaluated quantitatively using correlation coefficients. Figure 24 shows the correlation coefficients of the IBIs that were estimated from the radar signal and the ECG data. In this figure, we see that the proposed method gives the highest correlation coefficient when compared with the other two methods that do not use topological information. When averaged over the nine participants, the correlation coefficient of the proposed method is 0.975, whereas the coefficients of the other two methods are 0.903 and 0.929. The correlation coefficient is thus improved by using the topological information by margins of 8.0 and 4.9 % in comparison to the other two methods. This result also demonstrates that the proposed method is effective in the estimation of a dynamically changing HR. We therefore conclude that the topological information of the features is essential for accurate IBI estimation.
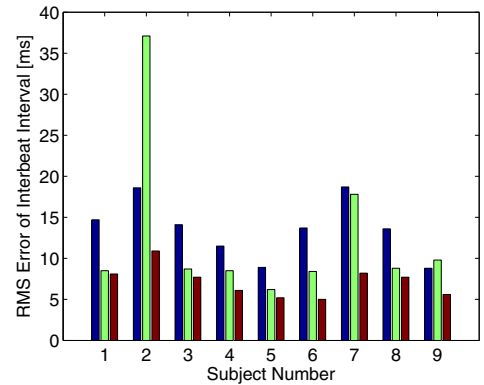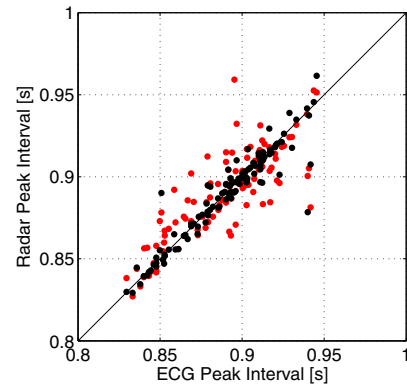
VIII. CONCLUSION

We have proposed an efficient and accurate method for instantaneous HR estimation using a UWB radar system. The proposed method uses the feature points found in radar signals to efficiently compute an approximate correlation function that is used to find associated feature pairs. This method enables quick correlation computation. In addition, we have introduced a new concept called feature topology, which uses the information of the feature sequence patterns, rather than the original waveform itself. We devised an appropriate mapping from the feature points to discrete complex numbers to evaluate the reproducibility of the feature sequences. Using the feature topology similarity, we can choose reliable feature points to improve the IBI estimation accuracy. The estimated IBIs were compared with the simultaneously measured ECG data to evaluate the accuracy of the proposed method. The results indicated the effectiveness of the proposed method, which worked well for the data of all nine participants. The next step in the course of this research is the extension of the proposed method to cases with respiration. Another important task in our future research will be to increase the number of
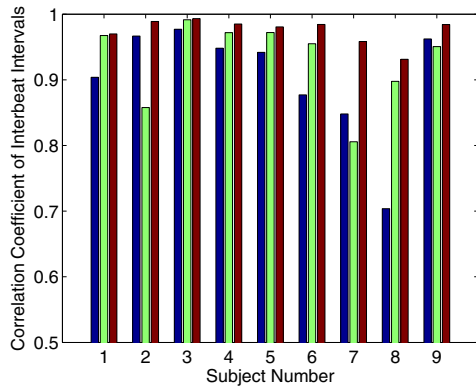
Fig. 24. Correlation coefficients of IBIs estimated from the radar signal and ECG data. The proposed method (in red) with $(\theta_c, \theta_t) = (0.1, 0.7)$, is compared with the correlation-based methods with $(\theta_c, \theta_t) = (0.1, 0.0)$ (in blue) and $(\theta_c, \theta_t) = (0.7, 0.0)$ (in green).

participants and select from a wider sample of the population that includes females, older people and subjects with higher BMI values to investigate the performance of the proposed method under various operating conditions.

REFERENCES

[1] B. Lohman et al., "A digital signal processor for Doppler radar sensing of vital signs," IEEE Eng. Med. Biol., vol. 21, no. 5, pp. 161–164, 2002.
[2] J. Kranjec et al., "Novel Methods for Noncontact Heart Rate Measurement: A Feasibility Study," IEEE Trans. Instrum. Meas., vol. 63, no. 4, pp. 838–847, 2014.
[3] B.-K. Park et al., "Arctangent demodulation with DC offset compensation in quadrature Doppler radar receiver systems," IEEE Trans. Microw. Theory, vol. 55, no. 5, pp. 1073–1079, 2007.
[4] W. Massagram et al., "Assessment of heart rate variability and respiratory sinus arrhythmia via Doppler radar," IEEE Trans. Microw. Theory, vol. 57, no. 10, pp. 2542–2549, 2009.
[5] G. Vinci et al., "Six-port radar sensor for remote respiration rate and heartbeat vital-sign monitoring," IEEE Trans. Microw. Theory, vol. 61, no. 5, pp. 2093–2100, 2013.
[6] A. Nezirovic et al., "Experimental study on human breathing cross section using UWB impulse radar," Proc. Radar Conf. 2008, 2008.

[7] J. Salmi and A. F. Molisch, "Propagation parameter estimation, modeling and measurements for ultrawideband MIMO radar," IEEE Trans. Antenn. Propag., vol. 59, no. 11, pp. 4257–4267, 2011.
[8] C. Li et al., "Experiment and spectral analysis of a low-power Ka-band heartbeat detector measuring from four sides of a human body," IEEE Trans. Microw. Theory, vol. 54, no. 12, pp. 4464–4471, 2006.
[9] P. Bernardi et al., "Design, realization, and test of a UWB radar sensor for breath activity monitoring," IEEE Sens. J., vol. 14, no. 2, pp. 584–596, 2014.
[10] M. Zakrzewski et al., "Comparison of center estimation algorithms for heart and respiration monitoring with microwave Doppler radar," IEEE Sens. J., vol. 12, no. 3, pp. 627–634, 2012.
[11] B. Schleicher et al., "IR-UWB radar demonstrator for ultra-fine movement detection and vital-sign monitoring," IEEE Trans. Microw. Theory Techn., vol. 61, no. 5, pp. 2076–2085, 2013.
[12] J. C. Y. Lai, et al., "Wireless Sensing of Human Respiratory Parameters by Low-Power Ultrawideband Impulse Radio Radar," IEEE Trans. Instrum. Meas., vol. 60, no. 3, pp. 928–938, 2011.
[13] J. Li et al., "Advanced signal processing for vital sign extraction with applications in UWB radar detection of trapped victims in complex environments," IEEE J. Sel. Top. Appl., vol. 7, no. 3, pp. 783–791, 2014.
[14] A. D. Droitcour et al., "Range correlation and I/Q performance benefits in single-chip silicon Doppler radars for noncontact cardiopulmonary monitoring," IEEE Trans. Microw. Theory Techn., vol. 52, no. 3, pp. 838–848, 2004.
[15] J. Li et al., "Through-wall detection of human being's movement by UWB radar," IEEE Geosci. Remote Sens., vol. 9, no. 6, 2012.
[16] W. Hu et al., "Noncontact accurate measurement of cardiopulmonary activity using a compact quadrature Doppler radar sensor," IEEE Trans. Biomed. Eng., vol. 61, no. 3, pp. 725–735, 2014.
[17] I. V. Mikhelson et al., "Remote sensing of heart rate and patterns of respiration on a stationary subject using 94-GHz millimeter-wave interferometry," IEEE Trans. Bio-med. Eng., vol. 58, no. 6, pp. 1671–1677, 2011.
[18] J.-H. Lee et al., "Noninvasive biosignal detection radar system using circular polarization," IEEE Trans. Inf. Technol. B., vol. 13, no. 3, pp. 400–404, 2009.
[19] K. C. Bilchick et al., "Prognostic value of heart rate variability in chronic congestive heart failure," Am. J. Cardiol., vol. 90, no. 24, pp. 24–28, 2002.
[20] D. Nagae and A. Mase, "Measurement of heart rate variability and stress evaluation by using microwave reflectometric vital signal sensing," Rev. Sci. Instrum., no. 81, 094301, 2010.
[21] S. Bakhtiari et al., "A real-time heart rate analysis for a remote millimeter wave I-Q sensor," IEEE Trans. Bio-med. Eng., vol. 5, no. 6, pp. 1839–1845, 2011.
[22] E. Conte et al., "ML period estimation with application to vital sign monitoring," IEEE Signal Proc. Let., vol. 17, no. 11, pp. 905–908, 2010.
[23] C. Lee et al., "Heart rate tracking using a Doppler radar with the reassigned joint time-frequency transform," IEEE Antenn. Wirel. Pr., vol. 10, pp. 1096–1099, 2011.
[24] C. Li et al., "Accurate Doppler radar noncontact vital sign detection using the RELAX algorithm," IEEE Trans. Instrum. Meas., vol. 59, no. 3, pp. 687–695, 2010.
[25] I. V. Mikhelson et al., "Noncontact millimeter-wave real-time detection and tracking of heart rate on an ambulatory subject," IEEE Trans. Inf. Technol. B., vol. 16, no. 5, Sep. 2012.
[26] M. Chen et al., "0.5-μm CMOS implementation of analog heart-rate extraction with a robust peak detector," IEEE Trans. Instrum. Meas., vol. 57, no. 4, pp. 690–698, 2008.
[27] T. Fukuda et al., "A 26GHz short-range UWB vehicular radar using 2.5cps spread spectrum modulation," Proc. IEEE/MTT-S Internationl Microwave Symposium, pp. 1311–1314, 2007.
[28] J. Wang et al., "1-D Microwave Imaging of Human Cardiac Motion: An Ab-Initio Investigation," IEEE Trans. Microw. Theory, vol. 61, no. 5, pp. 2101–2107, 2013.

Takuya Sakamoto (M'04) received the B.E. degree in electrical and electronic engineering from Kyoto University, Kyoto, Japan, in 2000 and the M.E. and Ph.D. degrees in communications and computer engineering from the Graduate School of Informatics, Kyoto University, in 2002 and 2005, respectively.

Since 2015, he has been an Associate Professor at the Graduate School of Engineering, University of Hyogo, Himeji, Japan. From 2006 through 2015, he was an Assistant Professor at the Graduate School of Informatics, Kyoto University. From 2011 through 2013, he was also a Visiting Researcher at Delft University of Technology, Delft, The Netherlands. His current research interests lie in ultra-wideband radar, radar imaging, and radar signal processing.

Dr. Sakamoto is a member of the Institute of Electronics, Information and Communication Engineers of Japan (IEICE), the Institute of Electrical Engineers of Japan (IEEJ), and the Japan Society of Ultrasonics in Medicine. He has been serving as an Accountant of IEEE AP-S Kansai Chapter since 2015. He received the Best Paper Award from the International Symposium on Antennas and Propagation (ISAP2004) in 2004, the Young Researcher's Award from the IEICE in 2007, the Best Presentation Award from the IEEJ in 2007, the Best Paper Award from the IEICE Communication Society in 2007, and the Best Paper Award from the International Symposium on Antennas and Propagation (ISAP2012) in 2012.

Ryohei Imasaka received his B.E. degree in electrical engineering from Kyoto University, Kyoto, Japan, in 2013. He is currently working toward his M.S. degree at the Graduate School of Informatics, Kyoto University. His research interests include vital monitoring technology using radar.

Hirofumi Taki received his M.D. and Ph.D. degrees in informatics from Kyoto University, Japan, in 2000 and 2007, respectively. He is currently a senior assistant professor of Graduate School of Biomedical Engineering at Tohoku University. His research interests include medical ultrasound, adaptive beamforming, and super-resolution imaging.

Toru Sato (M'92) received his B.E., M.E., and Ph.D. degrees in electrical engineering from Kyoto University, Kyoto, Japan in 1976, 1978, and 1982, respectively. He has been with Kyoto University since 1983 and is currently a Professor in the Department of Communications and Computer Engineering, Graduate School of Informatics. His major research interests include system design and signal processing aspects of UWB radars, atmospheric radars, radar remote sensing of the atmosphere, and biomedical imaging.

He is a fellow of the Institute of Electronics, Information, and Communication Engineers of Japan, and a member of the Society of Geomagnetism and Earth, Planetary and Space Sciences, the Japan Society for Aeronautical and Space Sciences, the Institute of Electrical and Electronics Engineers, and American Meteorological Society.

Mototaka Yoshioka received his B.S. and M.S. degrees in electrical and electronic engineering from Tokyo Institute of Technology, Tokyo, Japan, in 2001 and 2003, respectively. In 2003, he joined Advanced Technology Research Laboratory, Matsushita Electronics Corporation (currently Panasonic Corporation), Kyoto, Japan, where he has been engaged in the research and development of automotive navigation system, wearable sensor, and vital sensor. He passed the patent attorney examination in 2008. His research interests include signal processing of vital sign and wearable/noncontact bio-sensing system.

Kenichi Inoue received his B.S. and M.S. degrees in electronic science and engineering from Kyoto University, Kyoto, Japan, in 2000 and 2002, respectively. In 2002, he joined the Semiconductor Device Research Center, Semiconductor Company, Matsushita Electric Industrial Co. Ltd., Osaka, Japan, where he was working on semiconductor laser devices, sensor devices and sensor systems. Since 2009, he has been with Advanced Technology Research Laboratories, Panasonic Corporation, Kyoto, Japan, where he is involved in the research and development of UWB radar sensor systems and their applications. Mr. Inoue is a member of the Japan Society of Applied Physics and the Institute of Electronics, Information and Communication Engineers of Japan.

Takeshi Fukuda was born in Osaka, Japan, in 1969. He received his B.S. and M.S. degrees in Electronic Engineering from Osaka University, Suita, Japan, in 1993 and 1995, respectively. In 1995, he joined the Electronics Research Laboratory, Matsushita Electronics Corporation, Osaka, Japan, where he has been engaged in the research and development of microwave integrated circuits. Since 2009, he has been with Advanced Technology Research Laboratories, Panasonic Corporation, Kyoto, Japan. His current research interests are algorithms and RF architectures for high-resolution millimeter-wave radar systems.

Hiroyuki Sakai was born in Osaka, Japan. He received the B.S. and the M.S. degrees in electrical engineering from Osaka University, Osaka, Japan, in 1984 and 1986, respectively. In 1986, he joined the Semiconductor Research Center, Matsushita Electric Industrial Co., Ltd., Osaka, Japan, and was engaged in research and development of high-speed GaAs digital IC's. From 1991 to 1992, he took an active part in the development of GaAs RF IC's for very compact cellular phones. In 1993, he started to research and develop the mm-wave devices and its IC's. In 1995, he was transferred to Electronics Research Laboratory, Matsushita Electronics Corporation, Osaka, and continued his research and development of millimeter-wave devices, particularly a new millimeter-wave IC concept named millimeter-wave flip-chip IC (MFIC). From 1998 to 2000, he visited Stanford University, Stanford, CA, as a visiting scholar, expanded his research subjects to new Si-based RF devices and their integration technologies. He is currently a manager of Semiconductor Device Research Center, Panasonic Corporation, Kyoto, Japan. Mr. Sakai had been serving a secretary of the IEEE EDS Kansai Chapter from 2002 to 2003. He was a member of the Technical Program Committee of the IEEE International Solid-State Circuit Conference from 2002 to 2008.